Changes in the Area, Thickness, and Volume of the Thwaites 'B30' Iceberg Observed by Satellite Altimetry and Imagery

Anne Braakmann-Folgmann[1], Andrew Shepherd[1], Andy Ridout[2]

[1] Centre for Polar Observation and Modelling (CPOM), University of Leeds, Leeds, LS2 9JT, UK
5 [2] Centre for Polar Observation and Modelling (CPOM), University College London, London, UK

Correspondence to: Anne Braakmann-Folgmann (eeabr@leeds.ac.uk)

Abstract. Icebergs account for half of all ice loss from Antarctica and, once released, present a hazard to maritime operations. Their melting leads to a redistribution of cold fresh water around the Southern Ocean which, in turn, influences water circulation, promotes sea ice formation, and fosters primary production. In this study, we combine CryoSat-2 satellite

10 altimetry with MODIS and Sentinel-1 satellite imagery to track changes in the area, freeboard, thickness, and volume of the B30 tabular iceberg between 2012 and 2018. We track the iceberg elevation when it was attached to Thwaites Glacier and on a further 106 occasions after it calved using Level 1b CryoSat data, which ensures that measurements recorded in different modes and within different geographical zones are consistently processed. From these data, we mapped the icebergs freeboard and estimated its thickness taking snowfall and changes in snow and ice density into account. We

15 compute changes in freeboard and thickness relative to the initial average for each overpass and compare this time series to precisely located tracks using the satellite imagery. This comparison shows that our time series of iceberg freeboard change is in good agreement with the geolocated overpasses (correlation coefficient 0.87), and suggests that geolocation reduces the uncertainty by 1.6 m. We also demonstrate that the snow layer has a significant impact on iceberg thickness change. Changes in the iceberg area are measured by tracing its perimeter and we show that alternative estimates based on

20 arc lengths recorded in satellite altimetry profiles and on measurements of the semi-major and semi-minor axes also capture the trend, though with a 48 % overestimate and a 15 % underestimate, respectively. Since it calved, the area of B30 has decreased from 1500 +/- 60 to 426 +/- 27 km^2, its mean freeboard has fallen from 49.0 +/- 4.6 to 38.8 +/- 2.2 m, and its mean thickness has reduced from 315 ± 36 to 198 ± 14 m. The combined loss amounts to an 80 +/- 16 % reduction in volume, two thirds (69 ± 14 %) of which is due to fragmentation and the remainder (31 ± 11 %) is due to basal melting.

1 Introduction

Iceberg calving accounts for roughly half of all ice loss from Antarctica (Depoorter et al., 2013; Rignot et al., 2013). At any time about 50-90 large icebergs are tracked in the Southern Ocean containing 7 000 to 17 000 km^3 of ice in total (Tournadre et al., 2015). For maritime operators it is essential to know the location of icebergs in order to reduce the risk of collision (Bigg et al., 2018; Eik and Gudmestad, 2010). The thickness of an iceberg determines if and where it will ground on the seabed, which has implications for maritime operations as well as for marine geophysics. Iceberg thickness also influences a wide range of physical and biological interactions with the Antarctic environment. Grounded icebergs can, for example, alter the local ocean circulation (Grosfeld et al., 2001; Robinson and Williams, 2012), melting of the adjacent ice shelves (Robinson and Williams, 2012), and prevent local sea ice from breaking up (Nøst and Østerhus, 2013; Remy et al., 2008). This, in turn, can impact the local primary production(Arrigo et al., 2002; Remy et al., 2008) and pose an obstacle to penguin colonies on their way to their feeding grounds (Kooyman et al., 2007). Temporarily grounded icebergs leave plough marks on the sea floor which can be an important geological record (Wise et al., 2017), but also impact on marine benthic communities (Barnes, 2017; Gutt, 2001). Therefore, iceberg thickness is an important parameter. Changes in iceberg thickness are also important, because they control the quantity of cold fresh water and terrigenous nutrients released into the ocean as icebergs melt (Gladstone et al., 2001; Silva et al., 2006). The release of relatively cold fresh water facilitates sea ice growth (Bintanja et al., 2015; Merino et al., 2016), immediately lowers the sea surface temperature (Merino et al., 2016), and has been found to even influence ocean water down to 1500 m depth (Helly et al., 2011) as well as lead to upwelling of deep ocean properties (Jenkins, 1999). In terms of nutrients, icebergs have shown to be the main source of iron in the Southern Ocean (Laufkötter et al., 2018; Raiswell et al., 2016; Wu and Hou, 2017) and therefore foster primary production in the proximity of icebergs (Biddle et al., 2015; Duprat et al., 2016; Helly et al., 2011), which in turn increases the abundance of krill and seabirds (Joiris, 2018; Smith et al., 2007) around icebergs. Furthermore, a range of studies have demonstrated that including more realistic iceberg distributions, trajectories and volumes in climate models leads to a redistribution of fresh water and heat flux, which agrees better with observations than models that only include small icebergs or that treat iceberg discharge as coastal runoff (Jongma et al., 2009; Martin and Adcroft, 2010; Rackow et al., 2013; Schloesser et al., 2019). To investigate each of these processes and interrelations, knowledge of iceberg thickness and volume and their change over time is required (England et al., 2020; Merino et al., 2016). Moreover, monitoring iceberg melting also presents an opportunity to gain insights into the response of glacial ice to warmer environmental conditions, which may develop at ice shelf barriers in the future (Scambos et al., 2008; Shepherd et al., 2019).

The first detailed studies on iceberg melting were performed in the 1970's and 1980's, and were mainly based on laboratory experiments or ship-based observations (Hamley and Budd, 1986; Huppert and Josberger, 1980; Neshyba and Josberger,

1980; Russell-Head, 1980). These studies found that iceberg melting to first order is proportional to the water temperature and that breakage dominates over melting for large icebergs. More recently, for example Silva et al. (2006) and Jansen et al. (2007) modelled melting of giant icebergs and the associated fresh water fluxes. The latter found that melting does not only depend on ocean temperature, but also on iceberg drift speed and the surrounding ocean currents. Scambos et al.

60   (2008) installed a range of measurement tools including a GPS receiver, a pre-marked accumulation mast and buried bamboo poles observed with a camera on a large Antarctic iceberg to monitor melting. They differentiate between three kinds of mass loss: rift calving, edge wasting and rapid disintegration. While rift calving can occur at any time within the iceberg life cycle along pre-existing fractures, edge wasting is only observed outside the sea ice edge. Rapid disintegration is caused by surface melting and the formation of surface lakes.

65   The advent of satellite remote sensing greatly increased our capability to study icebergs. A wide range of studies have employed repeat satellite imagery to track changes in iceberg area (Bouhier et al., 2018; Budge and Long, 2018; Han et al., 2019; Li et al., 2018; Mazur et al., 2019; Scambos et al., 2008). The most common approach to measure iceberg thickness is using satellite altimeter measurements of their freeboard, which began in the late 1980's (McIntyre and Cudlip, 1987). Since then, a range of studies have employed laser and radar altimetry to study freeboard change: Jansen et al. (2007)

70   studied the A-38B iceberg in the Weddell and Scotia Sea with a combination of laser and radar altimetry, and Scambos et al. (2008) also include three Ice, Cloud and land Elevation Satellite (ICESat) overpasses over the A22A iceberg to derive its thickness change. Both studies make use of satellite imagery to geolocate the altimetry tracks and to compare similar areas in terms of freeboard change. In contrast, Tournadre et al. (2015) employ altimetry measurements from Envisat, Jason1 and Jason2 to analyse freeboard change of the C19A iceberg without any geolocation. Bouhier et al. (2018) analyse

75   thickness changes of the B17A and C19A icebergs in open water using altimetry data without geolocation, Li et al. (2018) calculate freeboard change of the C28A and C28B icebergs for two years at the intersections of CryoSat-2 overpasses, and Han et al. (2019) also used intersecting CryoSat-2 tracks to calculate freeboard change of the A68 iceberg in the Weddell Sea. When thickness and area changes are combined it is possible to detect changes in iceberg volume (Bouhier et al., 2018; Han et al., 2019; Tournadre et al., 2015). However, studies to date have been limited to selected icebergs, have

80   focussed on the Weddell Sea, and have employed a variety of approaches to account for the irregular sampling of altimetry tracks including manual geolocation of entire tracks relative to the initial surface (Jansen et al., 2007), geolocation of intersecting tracks (Han et al., 2019; Li et al., 2018), and with no geolocation at all (Bouhier et al., 2018; Tournadre et al., 2015). More recently, satellite stereo photogrammetry (Enderlin and Hamilton, 2014; Sulak et al., 2017) and interferometry (Dammann et al., 2019) have been employed to measure iceberg thickness and volume as an alternative approach, though

85   both methods are labour intensive. In this study, we quantify changes in the area, freeboard, thickness and volume of the B30 iceberg, which has been adrift in the Southern Ocean since it calved from the Thwaites Glacier 8.5 years ago (Budge

and Long, 2018; Fig. 1), and we also assess the agreement between estimates of freeboard change determined relative to the average initial surface and using precise geolocation with the aid of near-coincident satellite imagery. The next chapter introduces the remote sensing data used in this study and explains our methodology; the third chapter presents our results

90 on iceberg area, freeboard, thickness and volume change in turn and discusses our findings. We close with conclusions and a brief outlook in chapter four.

2 Data and Methods

To chart the iceberg area change over time we delineate its extent in a sequence of Moderate Resolution Imaging Spectroradiometer (MODIS) optical satellite imagery and Sentinel 1 synthetic aperture radar (SAR) satellite imagery. We

95 then use CryoSat-2 satellite radar altimetry to determine changes in the iceberg freeboard and thickness, assuming that it is floating in hydrostatic equilibrium, and making use of the iceberg orientation relative to its initial position using near-coincident satellite imagery on some occasions. We account for snow accumulation and model variations in snow and ice density when converting iceberg freeboard to thickness. Finally, we combine both data sets to estimate the iceberg's volume change over time.

100 ### 2.1 Iceberg location

We use daily archived iceberg positions from the Antarctic Iceberg Tracking (AIT) database provided by the Brigham Young University (Budge and Long, 2018) as a baseline estimate of the B30 iceberg location since it calved in 2012 (Fig. 1). The AIT database makes use of coarse-resolution passive microwave scatterometer imagery in which icebergs are manually detected and the central position is recorded daily. It includes icebergs longer than 6 km adrift in the Southern

105 Ocean between 1987 and 2019, augmented with estimates of position and the semi minor and major axes lengths of icebergs longer than 18.5 km that are tracked operationally by the U.S. National Ice Center (NIC) using a combination of visible, infrared and SAR imagery.

The Cryosphere
Discussions
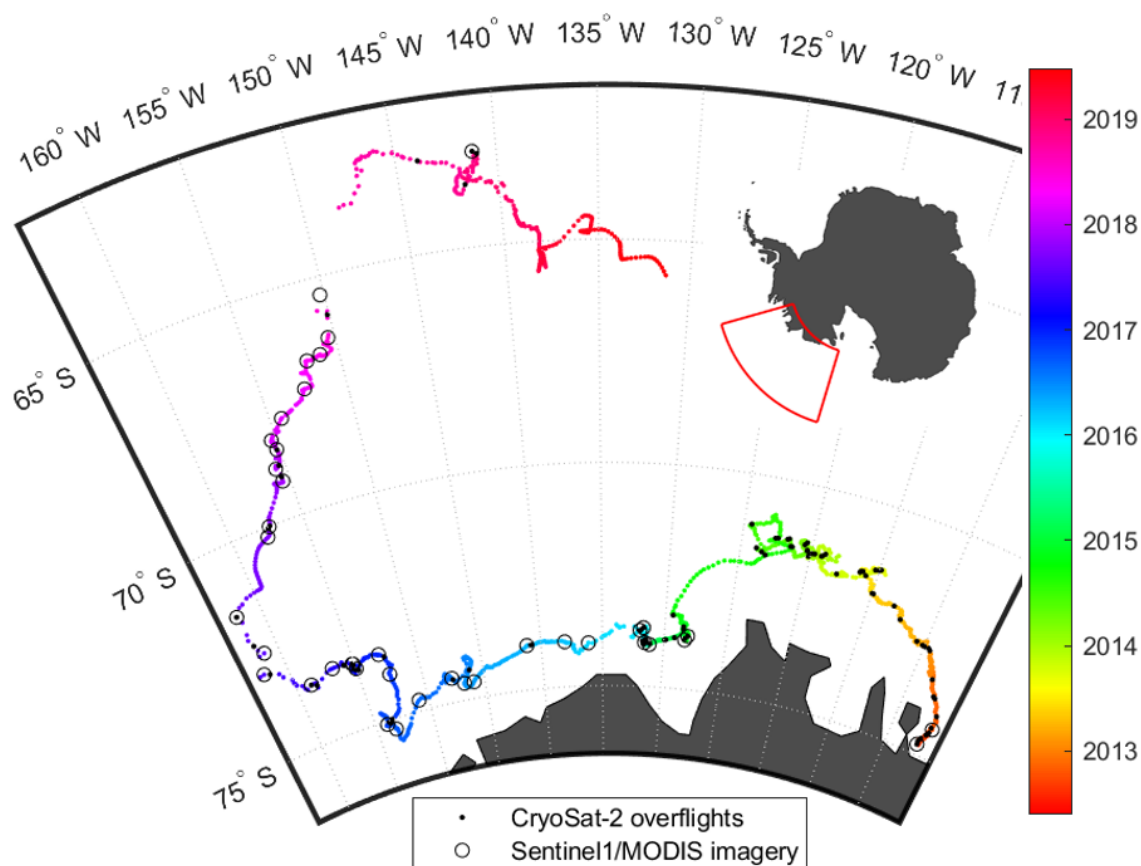
Figure 1: Trajectory of the B30 iceberg as recorded by the Antarctic Iceberg Tracking Database (Budge and Long, 2018): After calving from the Thwaites ice shelf in 2012, it followed the coastal current westwards, started drifting north in 2017 and eventually disintegrated in 2019. Black dots mark the positions where CryoSat-2 overflights over the iceberg are available, circles depict the positions of the MODIS and Sentinel 1 images used in this study

2.2 Initial iceberg shape, size and calving position

To determine the initial shape, size and calving position of B30, we use MODIS images acquired before and after the calving event to identify which section of the Thwaites ice shelf calved to form the iceberg. MODIS is an instrument on the Terra and Aqua satellites by NASA launched on 18th December 1999 and 4th May 2002, respectively. The instrument measures radiance in the visible and infrared range with a spatial resolution of 250 m to 1 km and covers the entire Earth in 1-2 days, though cloud occlusions and the absence of daylight reduce data availability for many applications. For this study we use bands 1 (red), 4 (green) and 3 (blue) of the MODIS Level 1B calibrated radiances at 500 m resolution (MOD02HKM). As B30 broke off on 24 May 2012 (Budge and Long, 2018) in Antarctic winter, during darkness, the

5

closest useful MODIS imagery is from the preceding autumn and subsequent spring. We use several MODIS images acquired in the subsequent spring after calving to determine the initial shape, as it is difficult to unambiguously distinguish the berg from clouds and sea ice in a single image. The initial perimeter (Figure 2a, 3a) was then shifted and rotated to fit

125   the situation before calving to identify the part of the Thwaites ice shelf that formed B30 (Fig. 4). The initial size of the iceberg is 1500 km^2.

2.3 Iceberg area

We employ three approaches to estimate the iceberg area; (i) manual delineation in sequential satellite imagery scenes, (ii) using measurements of the semi-major and semi-minor axes provided by the NIC and (iii) using measurements of their arc

130   lengths recorded in satellite altimetry. While manual delineation provides the most consistent and accurate area estimate, the axes and arc length approaches are much simpler to implement and can be fully automated.

Our main approach to determine iceberg area is manual delineation using a sequence of 32 Sentinel-1 SAR and 8 MODIS optical imagery. Sentinel 1A and 1B are companion imaging radar satellites launched by the European Space Agency on 3rd April 2014 and 25th April 2016, respectively. Together, they provide repeat sampling of the Earth's surface every 6

135   days. For this study, we use Level 1 Ground Range Detected (GRD) data. Depending on availability, both interferometric wide (IW) and extra wide (EW) swath mode are used, but over the open ocean only EW data are acquired. We employ the Sentinel Application Platform (SNAP) toolbox to apply the orbital and radiometric corrections. The SAR images were multi-looked with a factor of six to reduce speckle and computation time, leading to a spatial resolution of 240 m. Finally, a terrain correction was applied using the GETASSE30 (Global Earth Topography And Sea Surface Elevation at 30 arc

140   second resolution) digital elevation model. The resulting backscatter values are scaled between their 5th and 95th percentiles and translated to a polar stereographic projection. The MODIS optical imagery were required prior to the launch of Sentinel-1A in 2014.

To chart changes in the iceberg area over time, we delimit its outline as a polygon in each subsequent image (Fig. 2). When the iceberg is drifting in open water its outline can be detected automatically using boundary detection techniques.

145   However, in the presence of sea ice the iceberg could not be separated using this approach, and so we instead delimit its outline manually on such occasions. To estimate the accuracy of our delineations we shrink and expand the polygons by one pixel (500 m for MODIS images and 240 m for multi-looked Sentinel 1 images) and calculate the resulting difference in area. This gives a mean relative difference of 3.6 %.
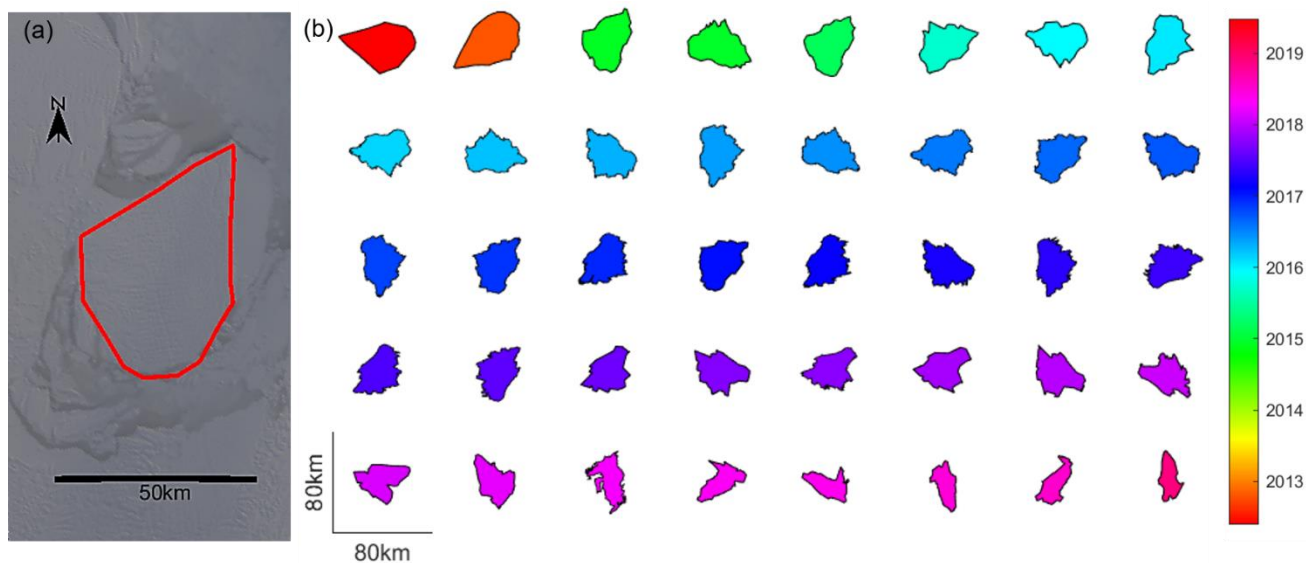
Figure 2: Outlines of the B30 iceberg derived from satellite imagery. a) Initial shape (red polygon) of the B30 iceberg determined from MODIS images after calving; the background is a MODIS image on 11 September 2012. b) Polygon outlines derived from further MODIS and Sentinel 1 imagery and used to calculate area change of the B30 iceberg.

Our second method of estimating the iceberg area is based on 228 measurements of the semi-major and semi-minor axes lengths. Although iceberg area is most accurately calculated from delineation of their full perimeter in satellite images, the downside of this approach is that it requires a high degree of time-consuming manual interaction and clear imagery. This also makes it less reproducible and subject to individual judgement. We estimate the size of an ellipse calculated from the semi major and minor axis provided by the NIC and compare this with our imagery-based iceberg area calculations. The NIC operationally tracks icebergs longer than 18.5 km using a combination of visible, infrared and SAR imagery. Observations are made weekly but especially in the early days longer data gaps exist and not every estimate of semi axes length is based on a new manual observation, but some are just duplicated from the previous observation. Their estimates of semi axes lengths are also rounded to nautical miles (1.852 km), leading to a stepwise evolution of iceberg area with only 8 different estimates. We base our trend estimate and analysis solely on these 8 estimates, because we are confident that these are unique observations. The uncertainty of this approach is governed by the assumption of an elliptical iceberg shape and the irregular, rounded updates.

Our third and final method of estimating the iceberg area is to make use of 106 CryoSat-2 satellite altimeter overpasses that record arc lengths of the iceberg and by assuming the iceberg has a circular shape. Depending on the position and relative orientation of the iceberg with respect to each overpass, CryoSat-2 will occasionally sample the long axis, but more often a shorter corner. This leads to significant variations in the area estimates, and in general an underestimation. We

employ a ten-point moving mean to reduce the variability. The principal uncertainty of this approach is because one-
170 dimensional arc lengths cannot reliably represent a two-dimensional area especially when the shape is evolving and if it is
unknown which part of the shape was sampled.

2.4 Iceberg orientation

To track the iceberg shape and rotation in later images relative to its initial orientation, we record the iceberg's orientation
in all satellite images that are near-coincident in time with CryoSat-2 overflights and therefore used for geolocation. To
175 orientate the iceberg, we manually click the coordinates of one corner of the initial iceberg polygon outline at the time of
each new overpass and adjust the rotation angle to align all images to a common orientation (Fig. 3). This allows us to
transform the iceberg coordinates at the time of each image acquisition relative to the equivalent position at the time just
before it calved.
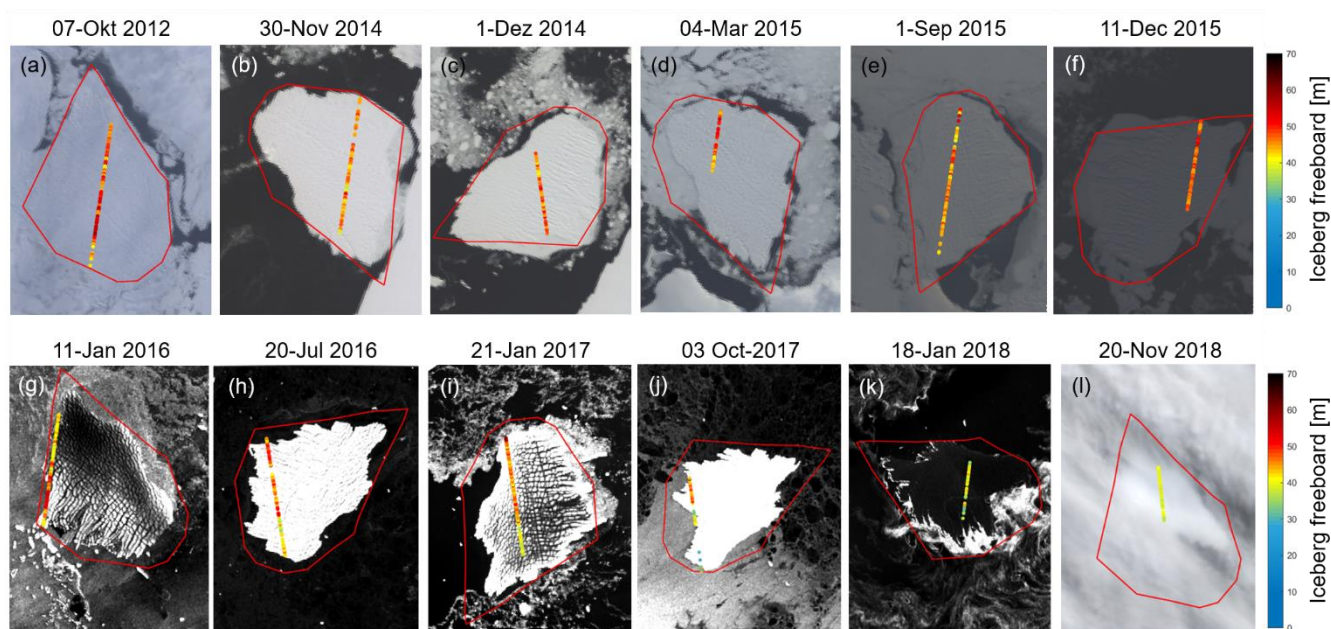
180

**Figure 3: Satellite imagery with near-coincident CryoSat-2 tracks of iceberg freeboard and the manually transformed initial
polygon shape plotted on top. The initial polygons are used to determine the relative position of each new overpass.**
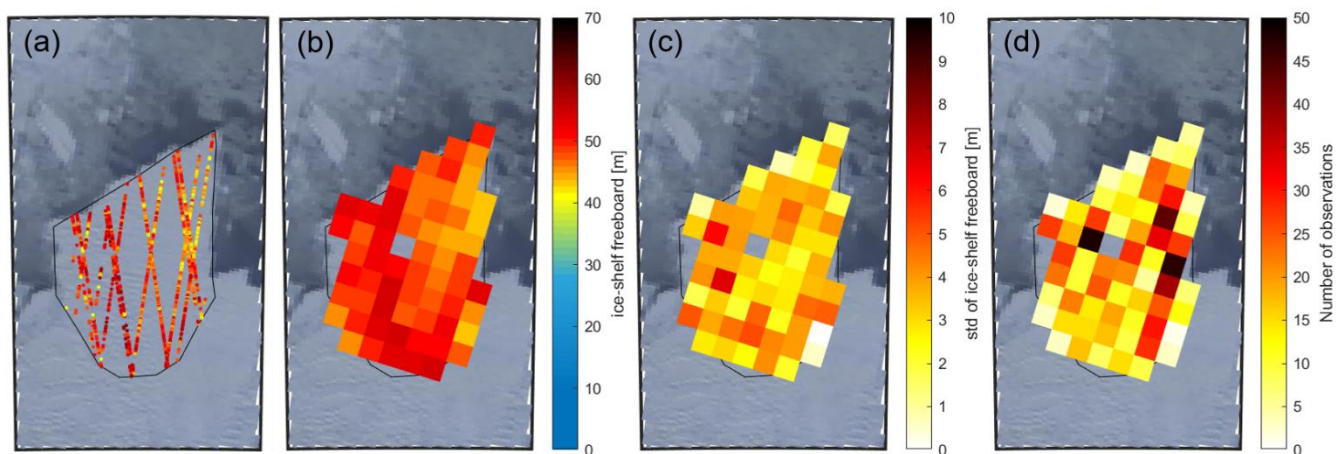
2.5 Initial iceberg freeboard

We use CryoSat-2 satellite altimetry to determine freeboard and thickness of the B30 iceberg. CryoSat-2 is a satellite radar
185 altimeter that employs SAR processing to achieve along track resolution of 250 m. It was launched by the European Space

Agency on 8 April 2010 in a 369-day repeat period with a 30-day sub cycle. We use Level 1B data from the CryoSat-2 Science server and apply the Centre for Polar Observation and Modelling sea ice processing system (Tilling et al., 2018) to deduce surface height. For consistency, a common threshold retracker is applied to measurements acquired in both SAR and SAR interferometric mode and over all surface types. Using Level 1B data is important, because the Level 2 products

190   are generated using different retrackers and using different biases for different modes and surface types, and so the signals acquired during different parts of the iceberg trajectory are not comparable. Iceberg freeboard is calculated by subtracting the adjacent mean sea surface height from the iceberg surface height.

Although satellite altimeters only sample icebergs along 1-dimensional profiles beneath their ground track while they are drifting, it is possible to build up a detailed 2-dimensional picture of their surface over time prior to calving while their

195   movement is relatively modest. To map the initial freeboard height of B30, we combine all CryoSat-2 tracks recorded within almost 5 months (1 January 2012 to 24 May 2012) before it calved (Fig. 4a). The Thwaites Glacier ice shelf flows at 3.9 km per year on average (Mouginot et al., 2019), and so we adjust earlier tracks to account for this movement. Because the ice shelf has rugged surface topography, the point-of-closest-approach (POCA) varies. To make different overpasses more comparable, we remove outliers by deleting freeboard heights greater than 60 m or below 20 m freeboard, and by

200   deleting freeboard heights falling either below the median minus one standard deviation or below the 5-point moving mean minus the 5-point moving standard deviation. The mean initial unfiltered iceberg freeboard is 45.5 m above the adjacent sea level with a wide spread of 8.1 m standard deviation. When crevasses are excluded, the mean freeboard is 49.0 m with a much lower standard deviation of 4.6 m. Because the resulting freeboard measurements are still quite sparse, we average them within 5 km grid cells to obtain a continuous reference surface (Fig. 4). The number and standard deviation of the

205   gridded freeboards give an indication of the variance within each grid cell. The mean standard deviation within each grid cell is 3.3 m, the standard deviation across different grid cells is 3.1 m and the overall standard deviation of all heights within the polygon is 4.6 m. We compare the gridded initial freeboard to measurements from the first CryoSat overpass when the iceberg is adrift, acquired shortly after calving, to check they are consistent, and find a mean difference of -0.4 m. As this value is significantly lower than the iceberg freeboard variability, we conclude that the ice shelf was floating freely

210   prior to calving also, and that the gridded heights are representative of the initial freeboard.

Figure 4: Initial freeboard heights of the B30 iceberg overlain on a MODIS image on 19 March 2012 (before calving). a) Filtered CryoSat-2 measurements of 145 days before calving, b) Gridded CryoSat-2 data, c) Standard deviation of the gridding, d) Number of measurements per grid cell

2.6 Iceberg freeboard change

When icebergs are adrift, their motion is sufficiently large to mean that they are only sampled in 1-dimensional profiles along satellite altimeter ground tracks (Fig. 3). We extract surface heights over the B30 iceberg when it is adrift (e.g. Fig. 5) using the position from the AIT database as an initial estimate of its location. However, because the AIT positions and timings are approximate and the iceberg has a significant extent, we investigate all CryoSat-2 ground tracks that pass within 1-degree latitude and 2-degrees longitude of the database position. Track segments are truncated to exclude altimeter echoes from targets where the first or last freeboard height is more than 3 m, to exclude measurements from the nearby continent, and we also exclude tracks that do not contain freeboard measurement between 20 and 60 m, to ensure that they sample the iceberg. We consider all freeboard heights between the first and last echo falling in the range 20 to 60 m as potential iceberg measurements (Tournadre et al., 2015). To avoid including adjacent icebergs or berg fragments, we exclude segments with more than 10 measurements of ocean or sea ice, identified as surface heights in the range -3 to +3 m, between potential iceberg measurements. We also remove crevasses and other rugged features using the same editing steps applied to determine the surface height prior to calving. As a final check, we calculate the distance of these remaining heights to the AIT database location, and discard measurements that are further away than half the iceberg length (28 km) to ensure we are tracking B30.

230   We apply two different techniques to calculate changes in the iceberg freeboard. For 12 tracks we are able to calculate precise changes in freeboard with spatial definition by making use of near-coincident satellite imagery to account for the rotation and translation of the iceberg relative to its initial position prior to calving and consider the estimated movement between the time of the nearest satellite image and altimeter acquisitions. At 94 other times, we compute the freeboard height change as the difference of mean freeboard from each new overpass relative to the initial mean surface height. While

235   these observations are of poorer certainty, they provide denser temporal sampling and fill gaps between the geolocated measurements. The first "co-location" method assigns both the initial heights and the new measurements to their closest 5 km grid cell and averages them to ensure that the same locations are compared. We account for the iceberg drift between the times of the satellite acquisitions, allowing a maximum separation of 72 hours (though most overpasses are separated by less than 24 hours). We assume a translational uncertainty of 3 km per day (Scambos et al., 2008) and a rotational

240   uncertainty of 15° per day. Both are scaled by the time difference between the image and the CryoSat overpass. We then perform a Monte Carlo simulation to assess how these positional uncertainties translate to uncertainty in freeboard change. This is combined with the standard deviation of the gridded CryoSat-2 freeboard data to yield an uncertainty estimate for the geolocated tracks. The second method ignores the relative position and orientation of the iceberg at the time of the altimeter overpasses, and simply compares the mean freeboard along each new track to the mean surface height before

245   calving. Although this method is easiest, since it does not rely on additional image data to locate the track, it cannot account for potential spatial variations in the iceberg freeboard. Because of this, we restrict the new overpasses to those including at least 20 measurements, as tracks sampling only the edges of an iceberg tend to be inaccurate. As uncertainty estimate we combine the standard deviation of each new overpass with the standard deviation of the initial height.
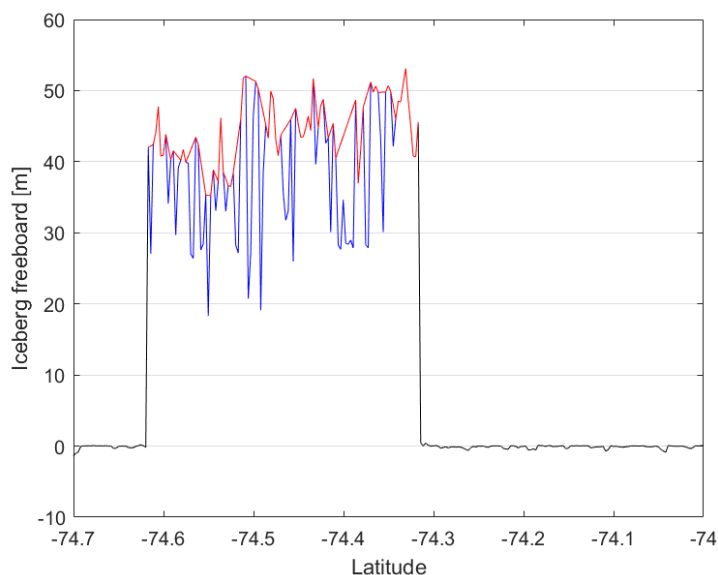
250 **Figure 5: Example of CryoSat-2 freeboard measurements along one track. The blue line shows which heights were identified as iceberg and the red line shows the remaining heights after filtering out crevasses.**

2.7 Iceberg thickness

We compute iceberg thickness H from our estimates of iceberg freeboard heights h_{fb} assuming hydrostatic equilibrium and that CryoSat-2 does not penetrate through the snow layer (Eq. 1; Moon et al., 2018). Besides these freeboard heights,

255 iceberg thickness also depends on column-average densities of sea-water ρ_w, ice ρ_i and snow ρ_s as well as snow depth h_s. Including a snow layer in this equation is important, because the snow layer adds to the observed freeboard and disguises a part of the ice freeboard change. On the other hand the additional load of the snow layer pushes the iceberg downwards. Both effects are taken into consideration. We assume sea-water density to be 1024 kg m^{-3} (Fichefet and Morales Maqueda, 1999) and set its uncertainty to 2 kg m^{-3}. Due to the long life cycle of the B30 iceberg of 6.5 years and the changing

260 environmental conditions it experiences during this time, we allow the ice and snow densities to evolve with time. Snow depth is also time-varying, and estimates of this and of snow and ice density are introduced successively.

$$H = \frac{\rho_w}{\rho_w - \rho_i} h_{fb} - \frac{(\rho_w - \rho_s)}{\rho_w - \rho_i} h_s \qquad (1)$$

To estimate the thickness of the snow layer, we download hourly ERA5 Reanalysis snowfall, snowmelt and snow evaporation data (Copernicus Climate Change Service, 2018), accumulate it daily and interpolate it in space and time to

265 the iceberg's trajectory. Snowmelt and snow evaporation are subtracted from the snowfall to retrieve the additional snow

accumulation since calving. However, this snow estimate does not account for snow being blown off the iceberg or onto the iceberg from the continent. To convert SWE to snow depth, we need to know snow density.

Snow density is time variable because snow compacts gradually during the iceberg's life time of several years as a function of snow depth h_s [m], the mean air temperature T [°C] and the mean wind speed v [m·s^{-1}] (Eq. 2; International Organization for Standardization, 1998). We use hourly ERA5 Reanalysis 2 m air temperature data and calculate wind speed from the ERA5 Reanalysis 10 m eastwards and northwards wind components (Copernicus Climate Change Service, 2018). Both are interpolated to the iceberg's trajectory and averaged since the day of calving. Because snow density depends on snow depth and snow depth depends on snow density, we calculate both iteratively starting with a snow density of 300 kg m^{-3}. We set the uncertainty in snow density to 50 kg m^{-3} (Kurtz and Markus, 2012) and the uncertainty in snow depth to 20%.

$$\rho_s = \left(90 + 130 \cdot \sqrt{h_s}\right) \cdot \left(1.5 + 0.17 \cdot \sqrt[3]{T}\right) \cdot \left(1 + 0.1 \cdot \sqrt{v}\right) \tag{2}$$

To calculate the iceberg's ice density profile we follow the approach by Tournadre et al. (2015), and determine two parameters V and R to fit the surface density and the depths of the critical density levels (550 kg m^{-3} and 830 kg m^{-3}) of the Thwaites Ice Shelf, from which it calved, as given in Ligtenberg et al. (2011; Eq. 3). ρ_g is the density of pure glacial ice (915 kg m^{-3}). Since the mean ice density depends on ice thickness and ice thickness depends on the mean ice density, we iterate over both equations. We also account for ice density changes over the iceberg's life cycle by calculating new mean densities as the iceberg thins. This incrementally reduces the average ice density as the densest ice is melted at the bottom. As ice density uncertainty we take 10 kg m^{-3}.

$$\rho_i = \frac{1}{H} \int_0^H \left(\rho_g - V \cdot e^{R \cdot z}\right) dz \tag{3}$$

## 3 Results and Discussion

We first assess changes in the B30 iceberg area using boundaries mapped from satellite imagery, and we compare the observed trend to more approximate estimates derived from arc-lengths and semi-major axes. Next, we determine the change in iceberg freeboard and we assess the impact of employing precise geolocation using near-coincident satellite imagery. Iceberg thickness changes are then computed from freeboard changes using time-varying estimates of snow accumulation and snow and ice densities derived from atmospheric reanalyses. Finally, iceberg area and thickness changes are combined to derive the change in volume and mass.

3.1 Iceberg Area Change

When the B30 iceberg first calved in May 2012, it was 1500 ± 60 km^2 large. Over the following 6.5 years it lost 1075 ± 66 km^2 of its extent, which corresponds to a 72 ± 11 % reduction at an average rate of 149 ± 5 km^2 per year (Fig. 6). However, because delineating iceberg outlines requires a high degree of time-consuming manual interaction, we also evaluate the efficacy of two alternative methods based on measurements of their orthogonal (semi-major and semi-minor) axes by the NIC and on arc lengths recorded in satellite altimetry which are considerably less laborious. Although these approaches also yield progressive reductions in area (Fig. 6), they exhibit significant positive (138 km^2, 14%) and negative (-426 km^2, 45%) biases, respectively, due to under-sampling of the iceberg geometry and the necessary approximation of a regular shape (ellipses and circles, respectively). While an ellipse overestimates the area compared to most shapes with the same axes, arc lengths yield an underestimate because corners are sampled more often than the major axis. One idea for improvement would be to use the maximum or to filter out tracks that only sample one corner, but the main problem remains that a one-dimensional length measurement cannot be translated into a reasonable area estimate without knowing the iceberg shape, which changes over time. Nevertheless, both the orthogonal axes and arc-length approaches yield area estimates that are reasonably well correlated (r>0.90) with those determined from our manual delineation. Area trends are overestimated by 16% and underestimated by 48%, respectively. While manual delineation provides the most consistent and most accurate area estimate, tracking iceberg axes or arc lengths yields area and area change estimates that are within 48% and is considerably less time consuming.
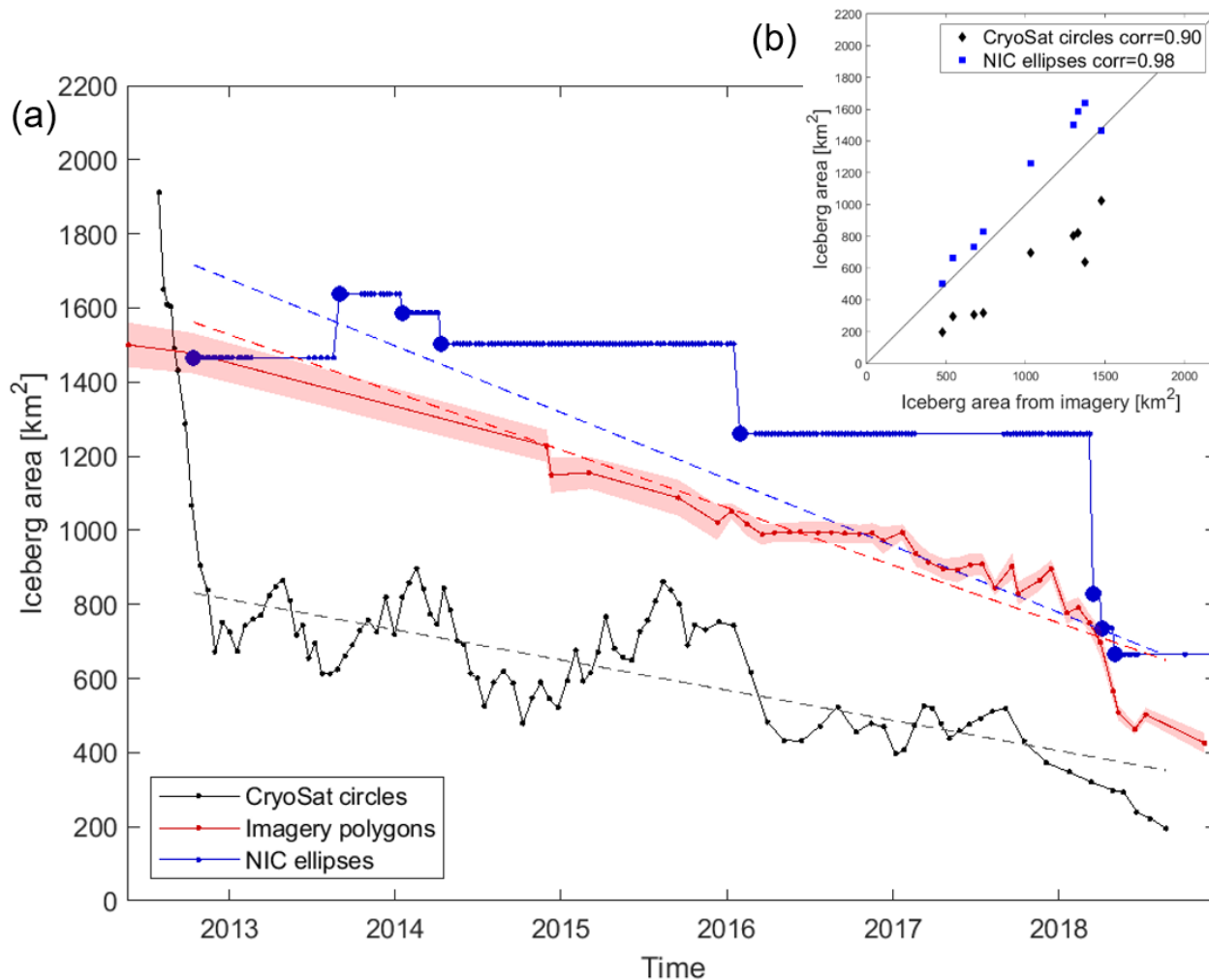
Figure 6: Area change of the B30 iceberg from polygons delineated in satellite imagery (red) and approximations using orthogonal axes provided by the National Ice Center (NIC) assuming an elliptical shape (blue) or using the arc lengths of CryoSat-2 overflights assuming a circular shape (black) over time (a) and as scatter plot. To fit the NIC trend line in (a) we only use unique values of orthogonal axes length (thick blue dots). These also define the dates of comparison in (b).

The rate of iceberg area loss from B30 was approximately constant until 2018, after which time it started to lose larger sections and more rapidly. Although its area has reduced steadily over time, it is less obvious which sections have been lost during individual calving events. However, by aligning the initial polygon to each subsequent image (Fig. 3) it is possible to identify when and where changes occur. The iceberg shape already appears altered on 30th November 2014, after bumping into the adjacent ice shelf which likely caused the first chunks to break off. B30 continued to lose smaller

15

320 sections along its edges over the next year – either through melting at the sides or smaller wastings – when it was drifting along the coastal current. In 2018 bigger sections are lost more rapidly, as the iceberg is drifting northwards in open water. Rift calving can occur at any time within an iceberg life cycle along pre-existing fractures (Scambos et al., 2008), while edge wasting is typically only observed when icebergs are travelling outside the sea ice pack. B30 was heavily crevassed prior to calving (e.g. visible in Fig. 3g and i), and so even the smaller wastings along its edges could reflect rift calving events rather than edge wastings. Another possibility is the 'footloose mechanism' (Wagner et al., 2014), which can become

325 a main driver of iceberg decay in warm waters when wave erosion at the waterline forms a sub-surface foot, creating a buoyancy stress that can lead to calving. Although it is not possible to investigate the effects of wave erosion using satellite data, the effect could in principle have caused the larger break-ups that occurred in 2018.

3.2 Iceberg Freeboard Change

To assess the change in freeboard over the survey period, we compare differences between the new overpasses and the

330 initial heights in space and time (Fig. 7). For the spatial analysis we chart the freeboard difference between each new geolocated overpass (Fig. 3) and the gridded initial height (Fig. 4b) at the same relative iceberg position. This comparison shows that the change in freeboard height across the iceberg is relatively homogenous at each epoch (Fig. 7a-l). We then average these differences per CryoSat-2 track and chart the variation over time alongside the less accurate (but more abundant) estimates determined without geolocation (Fig. 7m). Because the observations without geolocation are relatively

335 imprecise, we apply a 10-point moving mean to the data and we also fit a polynomial of 3rd order (and starting at zero) to model the trend. Overall, the B30 iceberg freeboard has reduced by 9.2 ± 2.2 m during the 6.5 years since it calved.

To assess the importance of geolocation, we compare freeboard changes calculated with and without this step (Fig. 7n). The estimates are well correlated (r=0.87) and the root mean square difference is 1.6 m, which is a measure of the improvement in certainty associated with geolocation and equal to the difference in mean uncertainty of geolocated tracks

340 (4.7 m) versus tracks without geolocation (6.3 m). Also, the temporal variation of freeboard changes computed from observations with and without geolocation are in good overall agreement (Figure 5a), and we conclude that for this iceberg we can combine the two and make use of the entire set of CryoSat-2 measurements. This finding should hold for other tabular icebergs where the topographic variability is smaller than the observed thinning. The variability of freeboards computed within each 5 km grid cell and across different grid cells are also of the same order – 3.3 m and 3.1 m, respectively

345 – and this is likely to have reduced the impact of geolocation uncertainties.
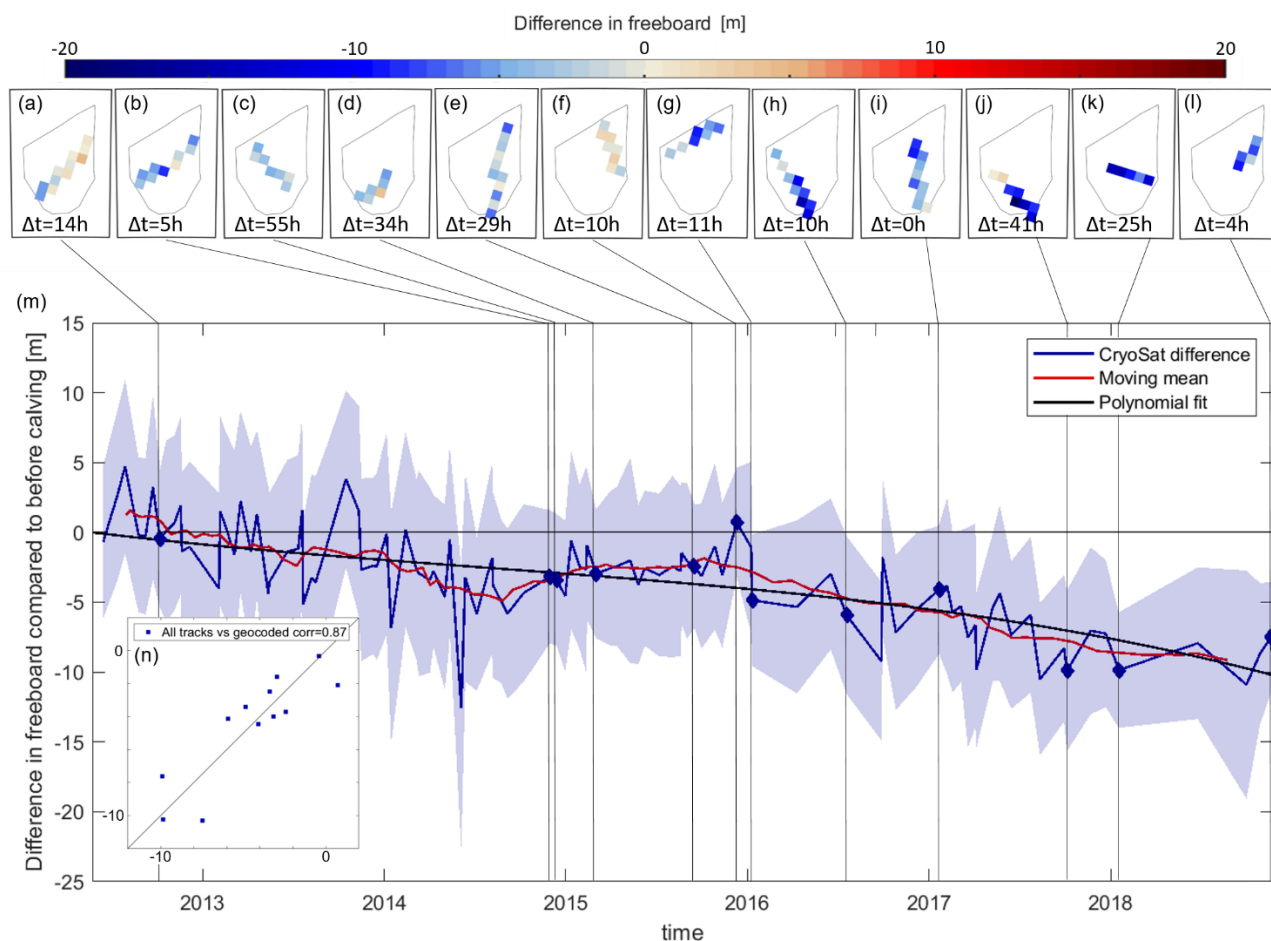
Figure 7: Freeboard change of the B30 iceberg. a) mean difference of each new overpass along time. CryoSat-2 tracks that have been geolocated are marked with a diamond, but all available CryoSat-2 overpasses have been used to calculate a moving mean and fit a polynomial; b-m) freeboard difference in each grid cell sampled by geolocated CryoSat-2 overpasses; the Δt values give the time difference between the CryoSat-2 overpass and the corresponding satellite image as an indication of the geolocation uncertainty due to iceberg drift; n) scatter plot of freeboard change from geolocated CryoSat-2 tracks versus the same tracks used without geolocation

3.3 Iceberg Thickness Change

We compute the iceberg thickness from our measurements of its freeboard (using the moving mean, red line in Fig. 7m) and by assuming that it is floating in hydrostatic equilibrium within the surrounding ocean with a surface snow layer. Accounting for the snow layer is important because it affects the ice freeboard and the iceberg buoyancy, and we take both effects into consideration. Based on hourly snowfall, evaporation and snowmelt derived from ERA5 reanalyses

17

(Copernicus Climate Change Service, 2018), we estimate that the iceberg accumulates 4.6 m of snow water equivalent during the 6.5 year survey period (Fig. 8). The rate of accumulation is quite linear. The iceberg thickness also depends on

360   densities of the snow layer, the iceberg, and the sea-water and we allow the snow layer and iceberg densities to evolve over time due to the changing environmental conditions it experiences during its long lifecycle. The mean iceberg density reduces from an initial estimate of 864 kg m^{-3} to a final value of 835 kg m^{-3} as a consequence of basal ice melting (Fig. 8a). The mean firn densification in West Antarctica has been estimated to be 2.78 cm per year on floating ice (Zwally et al., 2005); applying this rate gives a total of 18 cm after 6.5 years, which is significantly smaller than the observed freeboard

365   loss of 9.2 m, so we don't apply it. The snow layer compacts over time due to its accumulation and warming, and we estimate that its average density rises from 252 to 616 kg m^{-3} which yields a 7.2 m thick layer after 6.5 years (Fig. 8b). We also investigate the impact of surface thawing; although the iceberg surface does experience temperatures above freezing every summer and for a total of 218 degree hours (number of hours above zero degrees Celsius times the temperature above zero degrees Celsius) since calving (Fig. 8c), in situ observations (Scambos et al., 2008) suggest that this translates into

370   only 8 to 16 cm of snow melting and this has negligible impact on the iceberg freeboard.
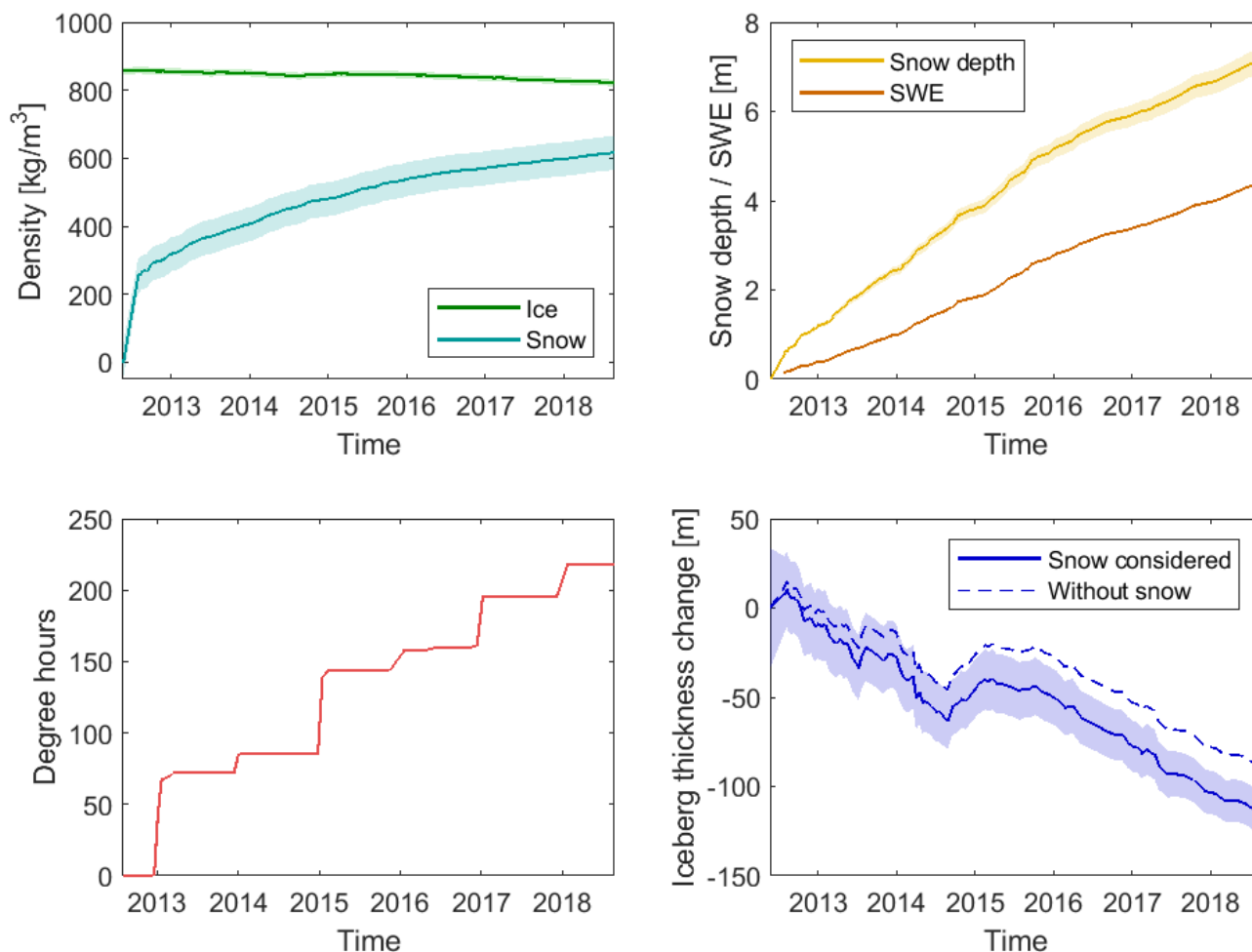
Figure 8: Evolution of the B30 iceberg properties: a) Ice density and snow density, b) Snow water equivalent (SWE) and snow depth accumulation on the B30 iceberg, c) Degree hours that the B30 iceberg experienced and d) Thickness change of the B30 iceberg with snow accumulation taken into consideration or without. Uncertainties are plotted as shaded areas.

We estimate the initial iceberg thickness to be 315 ± 36 m, on average, reducing to 198 ± 14 m after 6.5 years (Fig. 8d). This amounts to 117 ± 38 m of thinning at an average rate of 17.3 ± 1.8 m per year. Previous studies have recorded iceberg thinning rates of up to 10 m per year when drifting within the sea ice extent close to the coast (Han et al., 2019; Jansen et al., 2007; Li et al., 2018; Scambos et al., 2008) and much higher rates in excess of 20 m per year when in warmer open water (Hamley and Budd, 1986; Jansen et al., 2007; Li et al., 2018; Scambos et al., 2008; Tournadre et al., 2015). The B30 iceberg has spent most of its lifetime close to the coast (Fig. 1), and so our estimated average thinning rate is in line with the results from other studies. To assess the impact of including a snow layer in the thickness calculation, we also compute

19

thickness change assuming no snow has accumulated since calving (Fig. 8d); this scenario leads to an estimated 90 ± 39 m reduction in iceberg thickness, 23 % lower than the rate determined when the snow layer is included, which illustrates its

385 importance. Apart from the snow layer, the iceberg density is also a significant factor in our thickness change calculation, and while we have attempted to model the evolutions of ice density, snow density, snow accumulation and surface thawing, their uncertainties are difficult to quantify.

3.4 Iceberg Volume and Mass Change

Having calculated changes in the B30 iceberg thickness associated with snowfall and basal melting and changes in area

390 due to fragmentation, we combine both to determine the overall change in volume (Fig. 9). To do this, we multiply each thickness estimate (Fig. 8d) with the imagery-based area estimates (Fig. 6) interpolated to the times of the CryoSat-2 overpasses. The proportion of the total volume changes associated with melting and fragmentation are calculated by keeping area and thickness constant (and equal to their average), respectively. To compute changes in mass we multiply the volume change due to fragmentation by the column-average iceberg density at each point in time, because this ice is

395 lost at the sides. In contrast, we multiply the volume change due to basal melting by the density of pure ice (915 kg m^{-3}), since this ice is lost at the bottom where ice density is highest. The total mass change is the sum of both components. Uncertainties are calculated by propagating the uncertainties of thickness change, area change and ice density.

The initial volume of B30 at the time of its calving was 472 ± 57 km^3 and after 6.5 years it has lost 378 ± 57 km^3 of ice, corresponding to a 80 ± 16 % reduction. Fragmentation accounts for two thirds (69 ± 14 %) of the total volume loss and

400 basal melting is responsible for the remainder (31 ± 11 %). However, volume changes due to fragmentation become the dominant source of ice loss towards the end of our survey, consistent with previous findings (Bouhier et al., 2018). The two icebergs studied by Bouhier et al., (2018) also show similar fractions of ice loss due to fragmentation (60% for the B17a iceberg and 75% for the C19a iceberg). In terms of mass, the iceberg has lost 325 ± 44 Gt of ice in total at an average rate of 46 ± 4 Gt per year. The loss due to basal melting (106 ± 35 Gt) can be used as a lower estimate of the freshwater

405 flux from B30. Some of the mass lost due to changes in area - in particular melting at the sides and smaller edge wastings - will probably melt locally and add to the freshwater flux, but bigger calving events create smaller icebergs which can survive and travel on their own. To calculate the total freshwater flux, the melting of all fragments has to be considered.
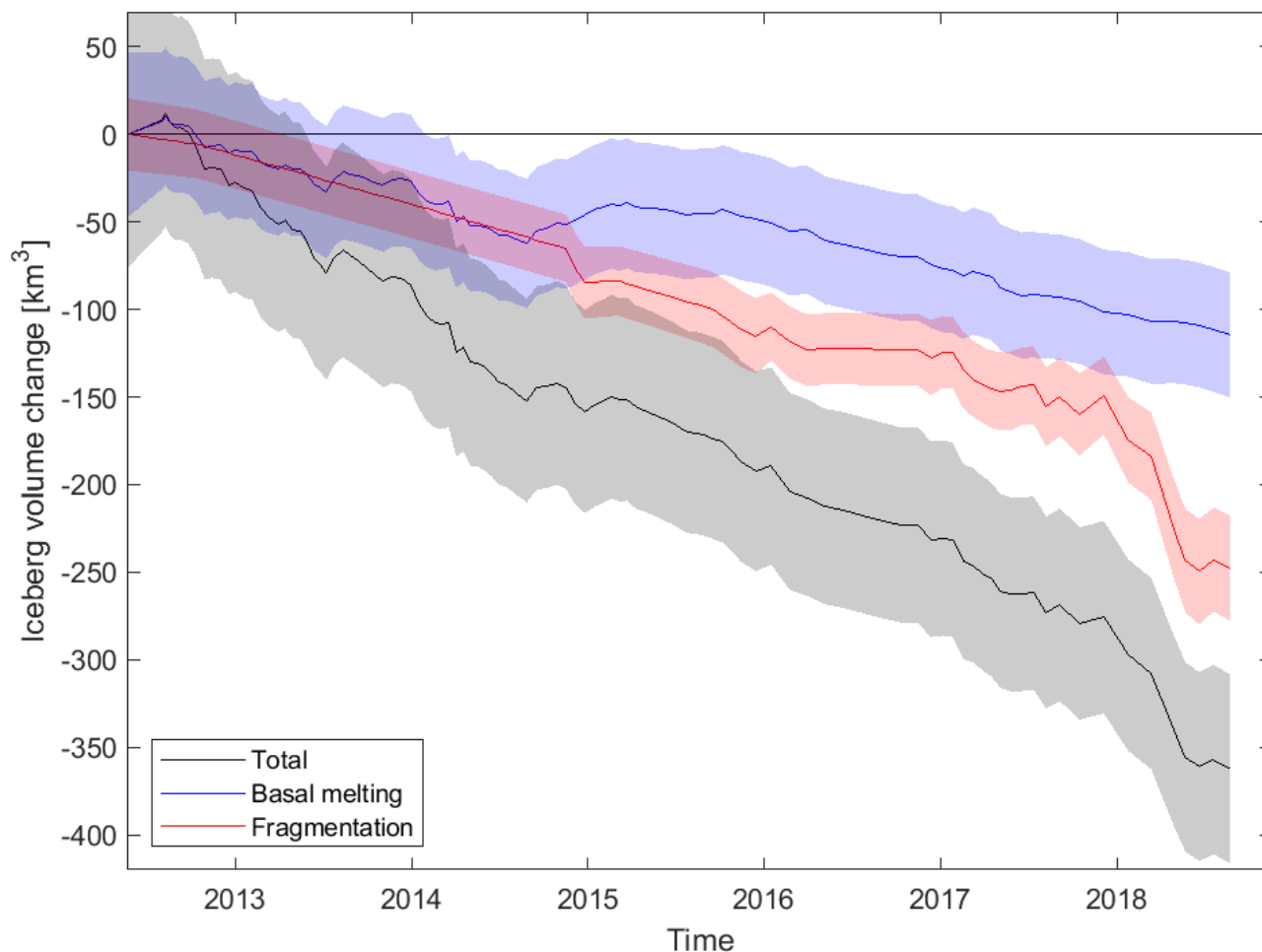
Figure 9: Volume change of the B30 iceberg divided into loss due to basal melting (thickness change, blue) and due to fragmentation (area change, red), as well as total volume loss (black).

4 Conclusions

In this study we have derived changes in the area, freeboard, thickness and volume of the B30 iceberg using a combination of satellite altimetry and satellite imagery. During the 6.5 years after the iceberg calved in May 2012, its area reduced from 1500 ± 60 km² to 426 ± 27 km² at an average rate of 149 ± 5 km² per year. The iceberg freeboard lowered by 9.2 ± 2.2 m over the same period. Using estimates of the snow accumulation and changes in snow and ice density, we estimate that the

21

iceberg thinned by 117 ± 38 m at a mean rate of 17.3 ± 1.8 m per year. Altogether, the iceberg lost 378 ± 57 km^3 of ice, and this equates to an estimated 325 ± 44 Gt reduction in mass.

We investigated the capability of automated approaches to approximate iceberg area and area change by comparing them to manually-derived estimates. Although the most reliable method of charting iceberg area change is through manual

420 delineation in satellite imagery, we show that less time-consuming estimates derived from measurements of the icebergs orthogonal axes or arc-lengths are also able to capture the area and area change over time, albeit with poorer certainty. Orthogonal axes lead to estimates of area and area trends that are 14 % and 16 % higher, respectively, and arc-lengths lead to estimates of area and area trends that are 45% and 48% lower, due to the necessary approximate of the iceberg shape.

We also presented a new thorough methodology to investigate iceberg freeboard and thickness change, using a densely

425 sampled time series of consistently processed Level 1 CryoSat data and assessed the importance of geolocation. Using a subset of 12 instances with geolocation, we find that omitting this step leads to a small deterioration in the certainty of detected freeboard change for the B30 iceberg, but the densely sampled time series is in good agreement with the geolocated tracks. We expect this finding also holds for other large tabular Antarctic icebergs with uniform topography, when the observed freeboard change exceeds the topography and when enough tracks are averaged. In this case, it suggests that the

430 procedure for tracking changes in iceberg thickness could be automated, given reliable estimates of their position (Budge and Long, 2018).

Finally, we developed a methodology to account for snowfall and variations in snow and ice density due to changing environmental conditions that large icebergs experience during their multi-annual drift. We found that the impact of snowfall on the retrieval of iceberg thickness increases over time, and after 6.5 years we estimate that 7.2 metres of snow

435 have accumulated which leads to a 27 m adjustment to the iceberg thickness change. Iceberg thickness change is also strongly dependent on the density profile which we derive from the depths of critical density levels (Ligtenberg et al., 2011), and so in situ observations would help to assess the reliability of this relationship. Likewise, direct measurements of the near-surface firn will help to assess the reliability of our reanalyses-based estimate of snow loading.

More icebergs - including the fragments lost from B30 - need to be studied to generalise the results we have and to constrain

440 both the fresh water flux, which influences water circulation (Grosfeld et al., 2001; Jenkins, 1999) and promotes sea ice formation (Bintanja et al., 2015; Merino et al., 2016), and input of terrigenous nutrients such as glacial iron into the Southern Ocean, which fosters primary production (Biddle et al., 2015; Duprat et al., 2016; Helly et al., 2011). Finally, studying icebergs as they drift through warmer water may give unique insights into the response of glacial ice to environmental conditions which may become commonplace at the ice shelf front in the future (Scambos et al., 2008;

445 Shepherd et al., 2019).

Author contributions

ABF and AS designed the study, AR processed the CryoSat elevations, ABF computed freeboard, area and volume change and prepared the figures, AS supervised the work. All authors contributed to the writing.

Competing interests

450   The authors declare that they have no conflict of interest.

Acknowledgements

455   **References**

Arrigo, K. R., Van Dijken, G. L., Ainley, D. G., Fahnestock, M. A. and Markus, T.: Ecological impact of a large Antarctic iceberg, Geophys. Res. Lett., 29(7), 8-1-8–4, https://doi.org/10.1029/2001GL014160, 2002.

Barnes, D. K. A.: Iceberg killing fields limit huge potential for benthic blue carbon in Antarctic shallows, Glob. Chang. Biol., 23(7), 2649–2659, https://doi.org/10.1111/gcb.13523, 2017.

460   Biddle, L. C., Kaiser, J., Heywood, K. J., Thompson, A. F. and Jenkins, A.: Ocean glider observations of iceberg-enhanced biological production in the northwestern Weddell Sea, Geophys. Res. Lett., 42(2), 459–465, https://doi.org/10.1002/2014GL062850, 2015.

Bigg, G. R., Cropper, T. E., O'Neill, C. K., Arnold, A. K., Fleming, A. H., Marsh, R., Ivchenko, V., Fournier, N., Osborne, M. and Stephens, R.: A model for assessing iceberg hazard, Nat. Hazards, 92(2), 1113–1136, 465   https://doi.org/10.1007/s11069-018-3243-x, 2018.

Bintanja, R., Van Oldenborgh, G. J. and Katsman, C. A.: The effect of increased fresh water from Antarctic ice shelves on future trends in Antarctic sea ice, Ann. Glaciol., 56(69), 120–126, https://doi.org/10.3189/2015AoG69A001, 2015.

Bouhier, N., Tournadre, J., Rémy, F. and Gourves-Cousin, R.: Melting and fragmentation laws from the evolution of two large Southern Ocean icebergs estimated from satellite data, Cryosphere, 12(7), 2267–2285, https://doi.org/10.5194/tc-470   12-2267-2018, 2018.

Budge, J. S. and Long, D. G.: A Comprehensive Database for Antarctic Iceberg Tracking Using Scatterometer Data, IEEE J. Sel. Top. Appl. Earth Obs. Remote Sens., 11(2), 434–442, https://doi.org/10.1109/JSTARS.2017.2784186, 2018.

Copernicus Climate Change Service, C.: ERA5 hourly data on single levels from 1979 to present, , https://doi.org/10.24381/cds.adbb2d47, 2018.

475   Dammann, D. O., Eriksson, L. E. B., Nghiem, S. V., Pettit, E. C., Kurtz, N. T., Sonntag, J. G., Busche, T. E., Meyer, F. J. and Mahoney, A. R.: Iceberg topography and volume classification using TanDEM-X interferometry, Cryosphere, 13(7), 1861–1875, https://doi.org/10.5194/tc-13-1861-2019, 2019.

Depoorter, M. A., Bamber, J. L., Griggs, J. A., Lenaerts, J. T. M., Ligtenberg, S. R. M., Van Den Broeke, M. R. and Moholdt, G.: Calving fluxes and basal melt rates of Antarctic ice shelves, Nature, 502(7469), 89–92, 480   https://doi.org/10.1038/nature12567, 2013.

Duprat, L. P. A. M., Bigg, G. R. and Wilton, D. J.: Enhanced Southern Ocean marine productivity due to fertilization by giant icebergs, Nat. Geosci., 9(3), 219–221, https://doi.org/10.1038/ngeo2633, 2016.

Eik, K. and Gudmestad, O. T.: Iceberg management and impact on design of offshore structures, Cold Reg. Sci. Technol., 63(1–2), 15–28, https://doi.org/10.1016/j.coldregions.2010.04.008, 2010.

485   Enderlin, E. M. and Hamilton, G. S.: Estimates of iceberg submarine melting from high-resolution digital elevation models: Application to Sermilik Fjord, East Greenland, J. Glaciol., 60(224), 1111–1116, https://doi.org/10.3189/2014JoG14J085, 2014.

England, M. R., Wagner, T. J. W. and Eisenman, I.: Modeling the breakup of tabular icebergs, Sci. Adv., 6(51), 1–9, https://doi.org/10.1126/sciadv.abd1273, 2020.

490   Fichefet, T. and Morales Maqueda, M. A.: Modelling the influence of snow accumulation and snow-ice formation on the seasonal cycle of the Antarctic sea-ice cover, Clim. Dyn., 15(4), 251–268, https://doi.org/10.1007/s003820050280, 1999.

Gladstone, R. M., Bigg, G. R. and Nicholls, K. W.: Iceberg trajectory modeling and meltwater injection in the Southern Ocean, J. Geophys. Res. Ocean., 106(C9), 19903–19915, https://doi.org/10.1029/2000jc000347, 2001.

495   Greene, C. A., Gwyther, D. E. and Blankenship, D. D.: Antarctic Mapping Tools for MATLAB, Comput. Geosci., 104, 151–157, https://doi.org/10.1016/j.cageo.2016.08.003, 2017.

Grosfeld, K., Schröder, M., Fahrbach, E., Gerdes, R. and Mackensen, A.: How iceberg calving and grounding change the circulation and hydrography in the Filchner Ice Shelf–Ocean System, J. Geophys. Res., 106(2000), 9039–9055, 2001.

Gutt, J.: On the direct impact of ice on marine benthic communities, a review, Polar Biol., 24(8), 553–564, 500   https://doi.org/10.1007/s003000100262, 2001.

Hamley, T. C. and Budd, W. F.: Antarctic Iceberg Distribution and Dissolution, J. Glaciol., 32(111), 242–251,

The Cryosphere
Discussions

Open Access

EGU

https://doi.org/10.1017/s0022143000015574, 1986.

Han, H., Lee, S., Kim, J. I., Kim, S. H. and Kim, H. C.: Changes in a giant iceberg created from the collapse of the Larsen C Ice Shelf, Antarctic Peninsula, derived from Sentinel-1 and CryoSat-2 data, Remote Sens., 11(4), 1–14,

505   https://doi.org/10.3390/rs11040404, 2019.

Helly, J. J., Kaufmann, R. S., Stephenson, G. R. and Vernet, M.: Cooling, dilution and mixing of ocean water by free-drifting icebergs in the Weddell Sea, Deep. Res. Part II Top. Stud. Oceanogr., 58(11–12), 1346–1363, https://doi.org/10.1016/j.dsr2.2010.11.010, 2011.

Huppert, H. E. and Josberger, E. G.: The Melting of Ice in Cold Stratified water, J. Phys. Oceanogr., 1980.

510   International Organization for Standardization, I.: ISO 4355 Bases for design on structures – Determination of snow loads on roofs., 1998.

Jansen, D., Schodlok, M. and Rack, W.: Basal melting of A-38B: A physical model constrained by satellite observations, Remote Sens. Environ., 111(2), 195–203, https://doi.org/10.1016/j.rse.2007.03.022, 2007.

Jenkins, A.: The impact of melting ice on ocean waters, J. Phys. Oceanogr., 29(9), 2370–2381,

515   https://doi.org/10.1175/1520-0485(1999)029<2370:TIOMIO>2.0.CO;2, 1999.

Joiris, C. R.: Seabird hotspots on icebergs in the Amundsen Sea, Antarctica, Polar Biol., 41(1), 111–114, https://doi.org/10.1007/s00300-017-2174-4, 2018.

Jongma, J. I., Driesschaert, E., Fichefet, T., Goosse, H. and Renssen, H.: The effect of dynamic-thermodynamic icebergs on the Southern Ocean climate in a three-dimensional model, Ocean Model., 26(1–2), 104–113,

520   https://doi.org/10.1016/j.ocemod.2008.09.007, 2009.

Kooyman, G. L., Ainley, D. G., Ballard, G. and Ponganis, P. J.: Effects of giant icebergs on two emperor penguin colonies in the Ross Sea, Antarctica, Antarct. Sci., 19(1), 31–38, https://doi.org/10.1017/S0954102007000065, 2007.

Kurtz, N. T. and Markus, T.: Satellite observations of Antarctic sea ice thickness and volume, J. Geophys. Res. Ocean., 117(8), 1–9, https://doi.org/10.1029/2012JC008141, 2012.

525   Laufkötter, C., Stern, A. A., John, J. G., Stock, C. A. and Dunne, J. P.: Glacial Iron Sources Stimulate the Southern Ocean Carbon Cycle, Geophys. Res. Lett., 45(24), 13,377-13,385, https://doi.org/10.1029/2018GL079797, 2018.

Li, T., Shokr, M., Liu, Y., Cheng, X., Li, T., Wang, F. and Hui, F.: Monitoring the tabular icebergs C28A and C28B calved from the Mertz Ice Tongue using radar remote sensing data, Remote Sens. Environ., 216(July 2017), 615–625, https://doi.org/10.1016/j.rse.2018.07.028, 2018.

530   Ligtenberg, S. R. M., Helsen, M. M. and Van Den Broeke, M. R.: An improved semi-empirical model for the densification of Antarctic firn, Cryosphere, 5(4), 809–819, https://doi.org/10.5194/tc-5-809-2011, 2011.

Martin, T. and Adcroft, A.: Parameterizing the fresh-water flux from land ice to ocean with interactive icebergs in a coupled

climate model, Ocean Model., 34(3–4), 111–124, https://doi.org/10.1016/j.ocemod.2010.05.001, 2010.

Mazur, A. K., Wåhlin, A. K. and Kalén, O.: The life cycle of small-to medium-sized icebergs in the Amundsen sea
535   embayment, Polar Res., 38, 1–17, https://doi.org/10.33265/polar.v38.3313, 2019.

McIntyre, N. F. and Cudlip, W.: Observation of a giant antarctic tabular iceberg by satellite radar altimetry, Polar Rec. (Gr.
    Brit)., 23(145), 458–462, https://doi.org/10.1017/S0032247400007610, 1987.

Merino, N., Le Sommer, J., Durand, G., Jourdain, N. C., Madec, G., Mathiot, P. and Tournadre, J.: Antarctic icebergs melt
    over the Southern Ocean : Climatology and impact on sea ice, Ocean Model., 104, 99–110,
540   https://doi.org/10.1016/j.ocemod.2016.05.001, 2016.

Moon, T., Sutherland, D. A., Carroll, D., Felikson, D., Kehrl, L. and Straneo, F.: Subsurface iceberg melt key to Greenland
    fjord freshwater budget, Nat. Geosci., 11(1), 49–54, https://doi.org/10.1038/s41561-017-0018-z, 2018.

Mouginot, J., Rignot, E. and Scheuchl, B.: Continent-Wide, Interferometric SAR Phase, Mapping of Antarctic Ice Velocity,
    Geophys. Res. Lett., 46(16), 9710–9718, https://doi.org/10.1029/2019GL083826, 2019.

545 Neshyba, S. and Josberger, E. G.: On the estimation of Antarctic iceberg melt rate, J. Phys. Oceanogr., 1980.

Nøst, O. A. and Østerhus, S.: Impact of Grounded Icebergs on the Hydrographic Conditions Near the Filchner Ice Shelf, ,
    75, 267–284, https://doi.org/10.1029/ar075p0267, 2013.

Rackow, T., Wesche, C., Timmermann, R., Hellmer, H. H., Juricke, S. and Jung, T.: A simulation of small to giant Antarctic
    iceberg evolution: Differential impact on climatology estimates, J. Geophys. Res. Ocean., 3170–3190,
550   https://doi.org/10.1002/2016JC012513.Received, 2013.

Raiswell, R., Hawkings, J. R., Benning, L. G., Baker, A. R., Death, R., Albani, S., Mahowald, N., Krom, M. D., Poulton,
    S. W., Wadham, J. and Tranter, M.: Potentially bioavailable iron delivery by iceberg-hosted sediments and atmospheric
    dust to the polar oceans, Biogeosciences, 13(13), 3887–3900, https://doi.org/10.5194/bg-13-3887-2016, 2016.

Remy, J. P., Becquevort, S., Haskell, T. G. and Tison, J. L.: Impact of the B-15 iceberg "stranding event" on the physical
555   and biological properties of sea ice in McMurdo Sound, Ross Sea, Antarctica, Antarct. Sci., 20(6), 593–604,
    https://doi.org/10.1017/S0954102008001284, 2008.

Rignot, E., Jacobs, S., Mouginot, J. and Scheuchl, B.: Ice-shelf melting around antarctica, Science (80-.)., 341(6143), 266–
    270, https://doi.org/10.1126/science.1235798, 2013.

Robinson, N. J. and Williams, M. J. M.: Iceberg-induced changes to polynya operation and regional oceanography in the
560   southern Ross Sea, Antarctica, from in situ observations, Antarct. Sci., 24(5), 514–526,
    https://doi.org/10.1017/S0954102012000296, 2012.

Russell-Head, D. S.: The Melting of Free-Drifting Icebergs, Ann. Glaciol., 1, 119–122,
    https://doi.org/10.3189/s0260305500017092, 1980.

Scambos, T., Ross, R., Bauer, R., Yermolin, Y., Skvarca, P., Long, D., Bohlander, J. and Haran, T.: Calving and ice-shelf
565   break-up processes investigated by proxy: Antarctic tabular iceberg evolution during northward drift, J. Glaciol.,
54(187), 579–591, https://doi.org/10.3189/002214308786570836, 2008.

Schloesser, F., Friedrich, T., Timmermann, A., DeConto, R. M. and Pollard, D.: Antarctic iceberg impacts on future
Southern Hemisphere climate, Nat. Clim. Chang., 9(9), 672–677, https://doi.org/10.1038/s41558-019-0546-1, 2019.

Shepherd, A., Gilbert, L., Muir, A. S., Konrad, H., McMillan, M., Slater, T., Briggs, K. H., Sundal, A. V., Hogg, A. E. and
570   Engdahl, M. E.: Trends in Antarctic Ice Sheet Elevation and Mass, Geophys. Res. Lett., 46(14), 8174–8183,
https://doi.org/10.1029/2019GL082182, 2019.

Silva, T. A. M., Bigg, G. R. and Nicholls, K. W.: Contribution of giant icebergs to the Southern Ocean freshwater flux, ,
111(July 2005), 1–8, https://doi.org/10.1029/2004JC002843, 2006.

Smith, K. L., Robison, B. H., Helly, J. J., Kaufmann, R. S., Ruhl, H. A., Shaw, T. J., Twining, B. S. and Vernet, M.: Free-
575   drifting icebergs: Hot spots of chemical and biological enrichment in the Weddell Sea, Science (80-.)., 317(5837),
478–482, https://doi.org/10.1126/science.1142834, 2007.

Sulak, D. J., Sutherland, D. A., Enderlin, E. M., Stearns, L. A. and Hamilton, G. S.: Iceberg properties and distributions in
three Greenlandic fjords using satellite imagery, Ann. Glaciol., 58(74), 92–106, https://doi.org/10.1017/aog.2017.5,
2017.

580 Tilling, R. L., Ridout, A. and Shepherd, A.: Estimating Arctic sea ice thickness and volume using CryoSat-2 radar altimeter
data, Adv. Sp. Res., 62(6), 1203–1225, https://doi.org/10.1016/j.asr.2017.10.051, 2018.

Tournadre, J., Bouhier, N., Girard-Ardhuin, F. and Remy, F.: Large icebergs characteristics from altimeter waveforms
analysis, J. Geophys. Res. Ocean., (Mcl), 2121–2128, https://doi.org/10.1002/jgrc.20224, 2015.

Wagner, T. J. W., Wadhams, P., Bates, R., Elosegui, P., Stern, A., Vella, D., Abrahamsen, E. P., Crawford, A. and Nicholls,
585   K. W.: The "footloose" mechanism: Iceberg decay from hydrostatic stresses, Geophys. Res. Lett., 41(15), 5522–5529,
https://doi.org/10.1002/2014GL060832, 2014.

Wise, M. G., Dowdeswell, J. A., Jakobsson, M. and Larter, R. D.: Evidence of marine ice-cliff instability in Pine Island
Bay from iceberg-keel plough marks, Nature, 550(7677), 506–510, https://doi.org/10.1038/nature24458, 2017.

Wu, S. Y. and Hou, S.: Impact of icebergs on net primary productivity in the Southern Ocean, Cryosphere, 11(2), 707–
590   722, https://doi.org/10.5194/tc-11-707-2017, 2017.

Zwally, H. J., Giovinetto, M. B., Li, J., Cornejo, H. G., Beckley, M. A., Brenner, A. C., Saba, J. L. and Yi, D.: Mass
changes of the Greenland and Antarctic ice sheets and shelves and contributions to sea-level rise: 1992-2002, J.
Glaciol., 51(175), 509–527, https://doi.org/10.3189/172756505781829007, 2005.